Research Article

Synthesis and Characterization of CeO$_2$/Ag$_3$PO$_4$ p-n Heterojunction Photocatalyst: Its Photocatalytic Activity for the Degradation of Alizarin Yellow Dye

Tigabu Bekele (ID)

Department of Chemistry, Mekdela Amba University, P.O. Box 32, Tulu Awulia, Ethiopia

Correspondence should be addressed to Tigabu Bekele; tgbekele19@gmail.com

Novel single and binary photocatalysts were synthesized by coprecipitation method. The crystal structure, surface area, morphology, bandgap energy, functional groups, and optical properties were characterized using XRD, BET, SEM-EDX, UV/vis, FTIR, and PL instruments, respectively. Aqueous solutions of the model contaminant alizarin yellow (AY) dye and real wastewater sample solutions were used to evaluate the photocatalytic activity of single and binary nanocomposite. We found that the photocatalytic activity of CeO$_2$/Ag$_3$PO$_4$ binary nanocomposite is higher than that of their individual counterparts. We investigated the effects of operating parameters such as pH, initial dye concentration, and photocatalytic loading on AY dye degradation. Under optimal conditions, the binary system showed an efficiency of 96.99%. The binary photocatalyst showed relatively higher AY photolysis efficiencies than actual wastewater, about 96.56% and 57.76%, respectively. The actions of various scavengers suggest that ·O$_2$ and ·OH scavengers play an important role in AY decomposition. When the reusability of the photocatalyst was tested, only a reduction of about 20% was observed after four consecutive runs. The degradation of AY follows pseudo-first-order kinetics for newly synthesized nanocomposite. This result indicates that the binary nanocomposite can serve as an excellent medium for electron transport.

1. Introduction

As a well-known contributor to environmental pollution, dyes are being removed from wastewater with greater frequency. They are typically resistant to light, water, oxidizing agents, and many chemicals, making it challenging to degrade them once released into the aquatic systems. Azo dyes are the most common and flexible category of organic dye-stuffs. The distribution of dyes and near-perfect color matching are two unavoidable constraints that frequently accompany dyeing. Sometimes dyeing is strategically modulated to confine and increase the relative number of dyes on the leather surface in order to reduce the consumption of dyes and processing costs. As a result of their intricate aromatic structures, azo dyes are both more stable and more challenging to eliminate from effluents released into water bodies [1, 2]. A variety of physical, chemical, and biological techniques have been reported with varying degrees of success for the treatment of all types of dyes.

Since they can address the issue of dye destruction in aqueous systems, advanced oxidation processes (AOPs), a contemporary technique, are used to degrade or remove those dyes. AOPs were found on the production of highly reactive species like hydroxyl radicals (·OH), which quickly and nonselectively oxidize a variety of pollutants. In order to lessen the color and organic load of effluent wastewaters that contain dyes, semiconductor-mediated photocatalysis has been investigated under a wide range of experimental conditions [3–5]. This is because there are AOPs that contain different mechanisms to degrade such dyes. Heterogeneous photocatalytic oxidation, also known as photocatalysis, is the most significant of those advanced oxidation processes [2, 6]. This method primarily deals with the oxidation of organic molecules and compounds using a solid metal oxide semiconductor as a catalyst, which is activated by the incidence of
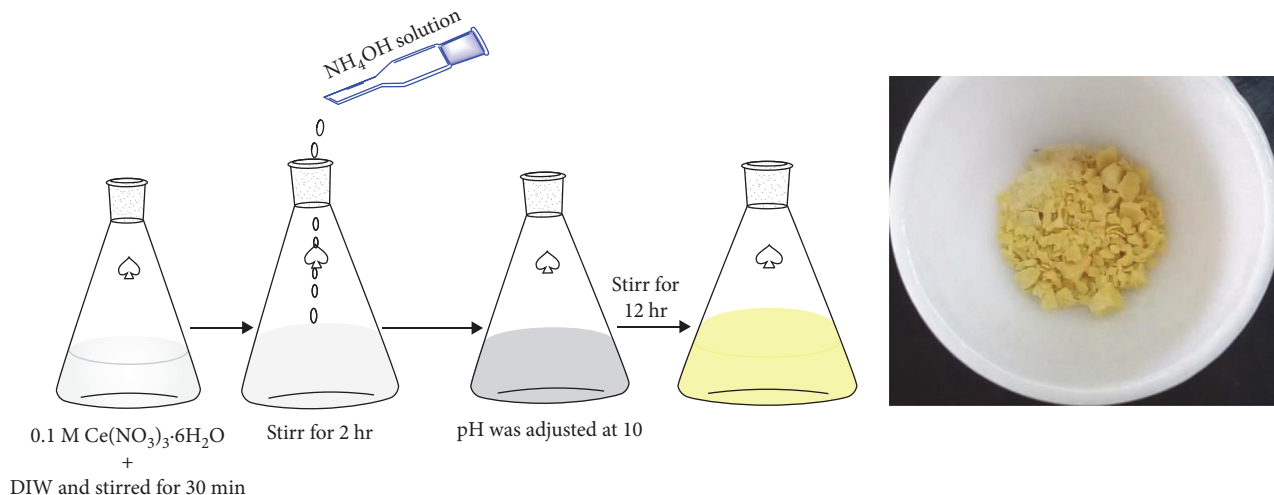
FIGURE 1: CeO$_2$ nanoparticle.

radiation at the right wavelength. When wastewaters are chemically treated by AOPs, the pollutants can completely mineralize and become simple, harmless byproducts like carbon dioxide, water, and inorganic salts. A semiconductor photocatalyst for water purification should ideally be UV or sunlight activated, photocatalytically active, chemically and biologically inert, and simple to produce and use [2, 7].

Semiconductor-based photocatalysts harnessing abundant sunlight are a promising approach to combat the global energy crisis and pollution [2, 8]. Ceria (CeO$_2$), an attractive rare-earth material and one of the best-known photocatalysts, has attracted a great deal of interest due to its high activity, low cost, and eco-friendly properties [9]. It shows promising photoactivation for oxidation of organic pollutants and water splitting for hydrogen generation. However, due to its large bandgap ($\sim$3.2 eV), pure CeO$_2$ can only be excited by ultraviolet (UV) light, limiting its further use in the visible light range. The visible light absorption of CeO$_2$ photocatalysts has been improved using various techniques such as doping, noble metal deposition, and composite formation to maximize the utilization of solar energy. Combining CeO$_2$ and another semiconductor into a composite is the most successful of these techniques [2, 10].

There are numerous reports on mixed metal oxides of CeO$_2$ that can enhance its thermal stability and photocatalytic performance. The photocatalytic activities of nanocomposite like TiO$_2$/CeO$_2$, CeO$_2$/ZnO, ZrO$_2$/CeO$_2$, and Fe$_2$O$_3$/CeO$_2$ under visible irradiation have been studied [11–14]. The main goal of this work is to synthesize binary CeO$_2$/Ag$_3$PO$_4$ and assess the photocatalytic activity of the nanocomposite in its as-synthesized state for the degradation of alizarin yellow (AY), a model pollutant dye.

2. Experimental Procedure

2.1. Synthesis of Photocatalysts

2.1.1. Preparation of CeO$_2$ Nanoparticle. As shown in Figure 1, the precipitation method was used to create cerium oxide nanoparticles. Cerium nitrate hexahydrate Ce(NO$_3$)$_3$·6H$_2$O

was prepared as an aqueous solution in 0.1 M deionized water (DIW) and stirred for 30 min. By adding dropwise amounts of aqueous NH$_4$OH solution while stirring continuously until precipitation was complete, the clear solution was precipitated. The reaction condition was then maintained at pH = 10 after two more hours of stirring. To finish the precipitation process, the reaction mixture was stirred for a further 12 hr. Following an hour of stirring, the ash-colored solution turned yellow. For 12 hr, the mixture was aged. The resulting yellow slurry was decanted, filtered, and washed numerous times with ethanol and deionized water. In order to encourage crystallization, the precipitate was oven dried at 140°C for 12 hr and then calcined at 500°C for 3 hr, as shown in Figure 1 [15, 16].

2.1.2. Preparation of Ag$_3$PO$_4$ Nanoparticle. A straightforward precipitation method [17] was used to create Ag$_3$PO$_4$ nanoparticles, as shown in Figure 2. In this common procedure, AgNO$_3$ and Na$_2$HPO$_4$ were separately dissolved in 60 mL of distilled water at an equal molarity (0.01 M). Following that, Na$_2$HPO$_4$ solution was gradually added to the AgNO$_3$ solution while magnetic stirring was ongoing for 4 hr. To obtain pure Ag$_3$PO$_4$ nanoparticle, the resulting yellow precipitate was collected, cleaned, and dried in an oven at 60°C for 6 hr. The final precipitate was then calcined at 300°C for 2 hr.

2.1.3. Synthesis of Ag$_3$PO$_4$/CeO$_2$ Nanocomposite. The fabrication of heterostructural complexes was performed by an *in situ* precipitation method, as shown in Figure 3 [18]. In a typical synthetic procedure, 0.0814 mmol of CeO$_2$ nanoparticles prepared by this method were dispersed in 100 mL of deionized water and sonicated for 30 min at a molar ratio of 1 : 1 [19]. Immediately after sonication, 0.1 M AgNO$_3$ aqueous solution was added to the white dispersed CeO$_2$ solution, followed by magnetic stirring for 30 min. An equimolar Na$_2$HPO$_4$ solution was then added dropwise with vigorous stirring for 2 hr. After that, the color of the solution changed from white to yellow. The precipitate was filtered, washed with deionized water and ethanol three times, and dried in an oven at 80°C for 10 hr.
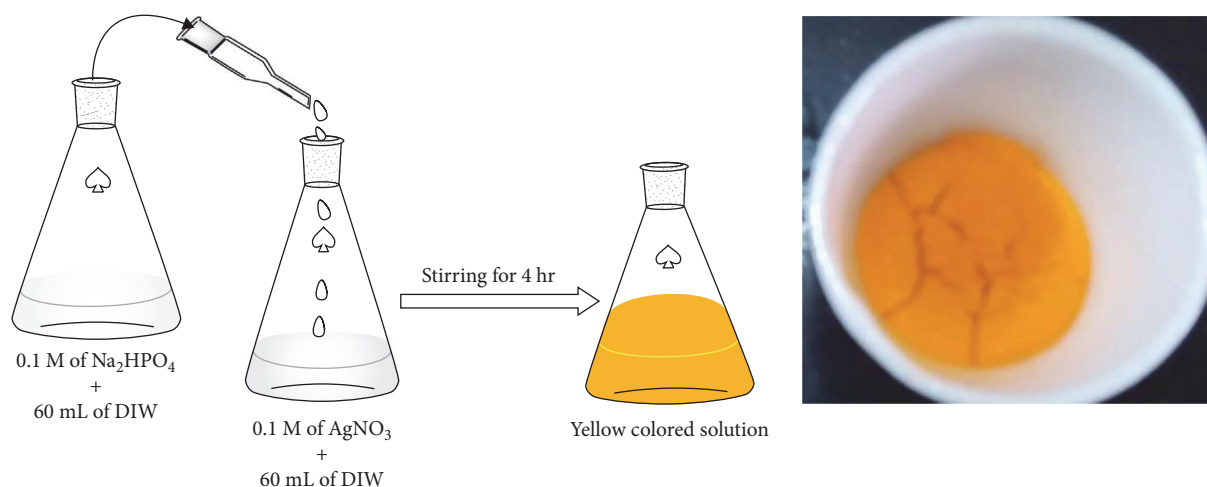
FIGURE 2: Synthesis of Ag$_3$PO$_4$ nanoparticle.
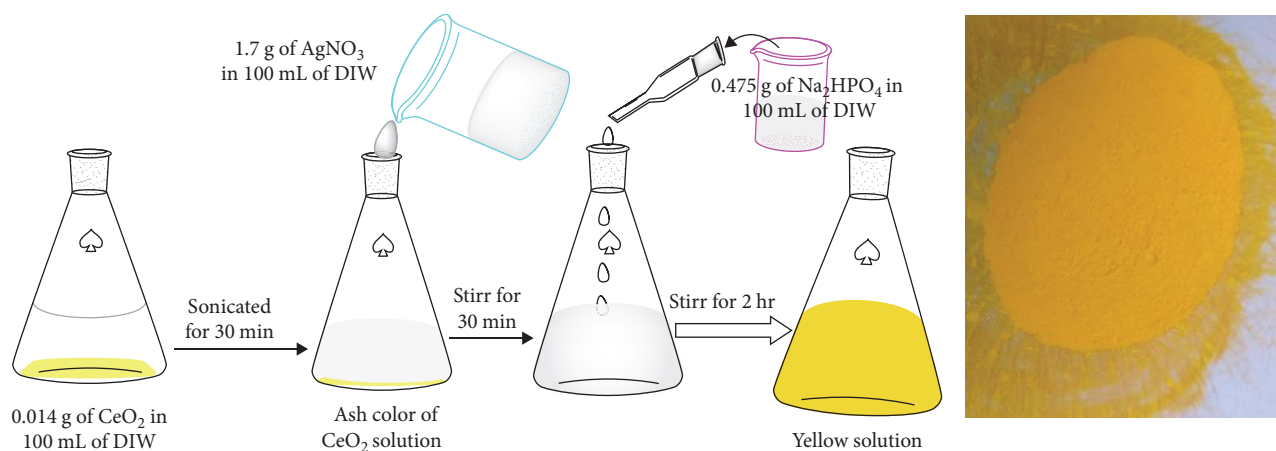
FIGURE 3: Synthesis of binary Ag$_3$PO$_4$/CeO$_2$ nanocomposite.

2.2. Characterization of the As-Synthesized Photocatalysts. The structures of all the as-synthesized photocatalyst were examined by XRD at room temperature at step scan rate of 0.02° (step time: 1 s; 2θ range: 5.0°–90.4°), which is equipped with an X-ray source of a CuKα radiation (wavelength of 0.15406 nm) using 45 kV accelerating voltage and 40 mA applied current. Finally, XRD patterns were collected with X'Pert Pro PAN alytical. The specific surface area of each of the as-synthesized photocatalyst was calculated from the N$_2$ adsorption–desorption isotherm at liquid-nitrogen temperature −196°C (77 K) and the micropore surface area was calculated by using the Brunauer–Emmett–Teller (BET) method.

Solid morphologies and particle distribution of the as-synthesized photocatalyst were determined by scanning electron micrographs (SEM Hitachi TM1000 with EDX detector) with a backscattered detector instrument; a gold film was sputtered into the sample prior to observation. From energy dispersive X-ray (EDX, an acquisition time (s) 40.0, process time 3 hr, and an accelerating voltage (kV) 15.0) link with SEM the elemental percent weight distribution of the as-synthesized sample was determined. The optical absorption

spectra and bandgaps of the as-synthesized photocatalysts were determined using UV–vis DRS. The solid-state absorbance of the photocatalyst was measured by scanning over the wavelength range of 200–800 nm.

The as-synthesized photocatalyst was characterized using FTIR (Spectrum 65, PerkinElmer) instrument. Dry mass of the photocatalyst was thoroughly mixed with a given dry mass of KBr and ground to a fine powder. A transparent disc was formed by applying a pressure in moisture free atmosphere. The IR absorption spectrum was recorded between 400 and 4,000 cm^{-1}. Photoluminescence (PL) spectra were measured using RF 5301PC Shimadzu photoluminescence. The spectra were obtained in the range of 250–650 nm.

2.3. Photocatalytic Degradation Studies. The photocatalytic activity of the whole as-synthesized sample was tested for degradation of the anionic dye AY in aqueous solution. For example, in a typical photocatalytic experiment, 10 mg/L AY was mixed with 0.20 g/L photocatalyst. The mixture was magnetically stirred for 1 hr in the dark to ensure adsorption/desorption equilibrium. Next, the suspension

was irradiated with visible light while being continuously stirred with a magnetic stirrer and the absorbance was measured at intervals of 20 min to monitor the decomposition reaction of the AY aqueous solution. A 300 W mercury lamp with an emission maximum at 355 nm was used as the UV light source and a 300 W fluorescent lamp was used as the visible light source. In this case, the UV component is removed with visible light during photocatalysis. The distance between the light source and dye solution is 30 cm. A pipette was used to flush air/oxygen into the solution during the procedure. Ten milliliters of suspension were then taken at 20 min intervals and centrifuged at 3,000 rpm for 10 min. Dye absorbance was measured using a UV/vis spectrophotometer at $\lambda_{\max}$ of the AY solution. Degradation rate (%) was calculated using the following formula [15, 20]:

$$\%\text{Degradation} = \frac{C_0 - C_t}{C_0} \times 100. \tag{1}$$

After kinetic analysis, we found that the photocatalytic degradation of organic pollutants follows the Langmuir–Hinshelwood mechanism and a pseudo-first-order reaction with a photocatalytic degradation rate (r) defined in [21]:

$$r = -\frac{dC(t)}{dt} = k_{\text{obs}} C(t), \tag{2}$$

when the concentration is very low, the observed rate constant, k_{obs} (min^{-1}) was determined from the simplified Langmuir–Hinshelwood model as given below [22]:

$$\text{Rate} = \ln(C_t/C_0) = -kt, \tag{3}$$

where k_{obs} is the observed rate constant in min^{-1}, C_t is the absorbance at a given time, C_0 is the absorbance at initial time, and t (min) is the reaction time. Hence, the linear fit between C_t/C_0 and irradiation time demonstrates the photocatalytic degradation rate. A higher k_{obs} value indicates a better photocatalytic activity of an investigated sample.

2.4. Effect of Operational Parameters on Photocatalytic Degradation.
Effects of operational parameters like initial pH, photocatalyst load, and initial concentration of organic compound (AY) were investigated for the binary CeO$_2$/Ag$_3$PO$_4$ photocatalyst in order to optimize the degradation efficiency.

2.4.1. Effect of pH.
The effect of pH on photocatalytic degradation of AY was investigated in the pH range of 2–10 by keeping photocatalyst load (0.2 g/L) and initial dye concentration (10 mg/L) constant. The desired pH level was achieved by the addition of (0.1/1 M) HNO$_3$ or (0.1/1 M) NaOH to the solution and the degradation efficiency of each pH was measured.

2.4.2. Effect of Initial Concentration of Organic Compound.
The effect of AY's initial concentration on the rate of photocatalytic degradation was observed by taking different initial concentrations of AY by keeping pH at 4 and photocatalyst load (0.2 g/L) constant.

2.4.3. Effect of Photocatalyst Load.
The effect of amount of photocatalyst on the rate of photocatalytic degradation of AY was observed by taking different amounts of the binary mixed oxide and keeping pH at 4 and initial dye concentration at 5 mg/L constant.

2.4.4. Effect of Active Species.
To evaluate the mechanism of photodegradation of CeO$_2$/Ag$_3$PO$_4$ binary nanocomposite by AY dye, the effect of the active species on the photodegradation process was investigated at an initial AY concentration of 5 mg/L, a photocatalyst of 0.15 g/L, and pH was evaluated at 4. The active species were determined by capture experiments using different scavengers, including NaHCO$_3$ as h$^+$ scavenger, His AgNO$_3$ as $\cdot$O$_2^-$ scavenger, and methanol as OH scavenger [51, 52]. Typically, 0.15 g/L photocatalyst and 15 mL of each scavenger of 0.1 M were added to 100 mL of 5 mg/L dye solution. The suspension was then irradiated with visible light for 160 min. Fifteen milliliters of suspension was collected at 30 min intervals and centrifuged at 3,000 rpm for 20 min. Dye absorbance was measured using UV/vis-DRS at $\lambda_{\max}$ of the AY solution. Finally, the degradation efficiency of photocatalyst versus dye can be calculated to determine the dominant role of the active species.

2.5. Stability Taste of the As-Synthesized Photocatalyst.
The recycling of the photocatalyst was carried out as follows [23]: the treated solution of the dye was centrifuged for 10 min to settle the catalyst after a first photodegradation cycle of a 5 mg/L solution of AY dye using 0.15 g/L of the as-synthesized photocatalyst and 160 min irradiation time. The solid phase containing the photocatalyst was carefully separated for reuse once the liquid phase had been filtered. The recovered photocatalyst was thoroughly cleaned with ethanol and deionized water. The photocatalyst was then reintroduced into a new cycle after being dried in an oven for 12 hr at 100°C in preparation for the following catalytic cycle. Four times the procedure was carried out. At 20 min, the 10 mL suspension was removed [15].

2.6. Dye Removal from Wastewater.
Wastewater collected from Kombolcha Textile Company was treated/decolorized using CeO$_2$/Ag$_3$PO$_4$ binary nanocomposite under optimized visible light irradiation conditions. Experiments were performed by taking a 100 mL sample of wastewater into a 250 mL beaker and adjusting its pH to 4. Then, 0.15 g/L of photocatalyst was added to the solution and the suspension was continuously stirred for 1 hr in the dark to allow the AY solution to reach adsorption/desorption equilibrium. Finally, the absorbance was measured by illuminating the suspension with visible light and aspirating 10 mL of the suspension at 20 min intervals for 160 min while stirring was continued. A plot of C_t/C_0 against exposure time was then plotted.
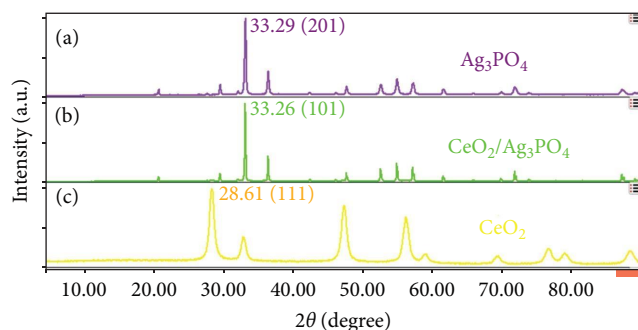
FIGURE 4: XRD spectra of (a) Ag_3PO_4, (b) CeO_2/Ag_3PO_4, and (c) CeO_2 photocatalysts.

3. Results and Discussion

3.1. Characterization of the As-Synthesized Photocatalysts

3.1.1. XRD Analysis. Figure 4 depicts the distinctive peaks on the XRD patterns of the as-produced photocatalyst: CeO_2, Ag_3PO_4, and CeO_2/Ag_3PO_4. Accordingly, the cubic fluorite structure of CeO_2 is represented by the diffraction peaks at scattering angles observed at 2θ of 28.61°, 32.69°, 48.09°, 57.75°, 58.99°, 69.16°, 77.01°, 79.66°, and 89.04°, which correspond to (111), (200), (202), (311), (222), (400), (313), (402), and (422) lattice planes [24]. The crystal planes (101), (020), (201), (121), (202), (302), (312), (040), (402), (412), (323), and (512) indexed to the body-centered cubic structure of Ag_3PO_4 are responsible for the diffraction peaks observed at 2θ of 21.01°, 30.06°, 33.29°, 36.14°, 43.00°, 48.02°, 53.00°, 54.88°, 57.17°, and 74.04° [25]. The CeO_2/Ag_3PO_4 composite's XRD pattern shows that the diffraction peak positions of CeO_2 have very weak intensities, which may be caused by the trace amounts of CeO_2.

The average crystallite size of each of the as-synthesized photocatalyst was calculated using the Debye–Scherrer formula [26]:

$$D = \frac{K\lambda}{\beta \cos \theta}, \tag{4}$$

where D is the crystallite size in nm, K is the shape factor constant taken as 0.9, β is the full width at half maximum (FWHM) in radians, λ is the wavelength of the X-ray (0.15406 nm) for Cu target Kα1 radiation, and θ is the Bragg's angle.

Table 1's summary of the calculated average crystalline size of the as-synthesized photocatalyst confirms the presence of good crystalline nano range between 10 and 45 nm. One of the crucial elements in the process of photocatalytic degradation is the photocatalysts crystallite size [27]. The photocatalytic degradation of AY by binary mixed oxide increases as the particle size decreases, as can be seen. This is because more active sites are formed on the photocatalyst surface, which leads to an increase in hydroxyl and superoxide radical production. Recombination of the electron–hole pair is less likely when particle size decreases. This is due to the possibility of increasing the distance needed for charge

carriers to migrate to the surface. As a result, binary mixed oxide with a crystal size of 40 nm was chosen and put to use in additional applications.

3.1.2. Determination of Surface Area (BET). The surface area of the nanocomposite as it was created was calculated using the Brunauer–Emmett–Teller (BET) method. The nitrogen adsorption–desorption isotherm analysis sample surface areas are displayed in Table 1 for each sample. The specific surface area of CeO_2 is 68 m^2g^{-1}, while Ag_3PO_4 is 10.021 m^2g^{-1}, demonstrating the latter's compacted nature. According to calculations, the specific surface area of the binary system CeO_2/Ag_3PO_4 was about 6 m^2g^{-1} [28]. Regarding composition and specific surface area across all the as-synthesized materials, there was generally no discernible pattern.

3.1.3. SEM-EDX Image Study. The investigation of the morphological images of the photocatalysts created in this way, CeO_2, Ag_3PO_4, and CeO_2/Ag_3PO_4, is depicted in Figure 5(a)–5(c). Every relevant component is present in every photocatalyst, as shown by the EDX spectrum. The morphology of the CeO_2 nanoparticles is seen to be almost spherical with slight agglomeration in the SEM images depicted in Figure 5(a). Figure 5(b) depicts the SEM image of an Ag_3PO_4 nanoparticle produced in the state, which reveals the presence of irregular particles with varying sizes and no clear morphology [29]. The average stoichiometric composition of Ag_3PO_4 nanoparticles, as determined by the EDX spectrum, is 92.60% silver and 7.40% phosphorus.

The CeO_2/Ag_3PO_4 composite has two distinct phases, as shown by the SEM image in Figure 5(c). CeO_2 is the substance that gives the sphere-shaped spots their shape. It is evident that the CeO_2 nanoparticles are evenly distributed throughout the Ag_3PO_4 crystallite sea, with the remaining Ag_3PO_4 particles acting as a core coating. Ag_3PO_4/CeO_2 nanoparticles have an average stoichiometric composition of 83.70% silver, 7.10% phosphorus, and 9.20% cerium, as determined by the EDX spectrum [24, 25]. It is interesting to note that the binary CeO_2/Ag_3PO_4 EDX spectrum exhibits Ce, Ag, and P peaks, which indicate the presence of CeO_2 and Ag_3PO_4 nanoparticles.

3.1.4. UV–Vis DRS Spectra. From a plot of absorbance against wavelength, the UV/vis diffuse absorption edges of the photocatalysts as-produced are obtained. The value of diffuse absorption edge (nm) is determined by the intercept of the tangent line on the descending portion of the absorption peak at the wavelength axis. In this scenario, Equation (5) was used to determine the bandgap energy (E_g) of the photocatalysts as-synthesized [30].

$$E_g = \frac{1240 \text{ eV}}{\lambda_{\max}}, \tag{5}$$

where E_g is bandgap energy in electron volts and $\lambda_{\max}$ is wavelength (nm) corresponding to absorption edge.

However, when the peak is not well resolved for the samples, the above method of bandgap estimation occasionally may not provide a clear tangential line. Diffuse reflectance measurements of dry powders can be carried out to get

TABLE 1: Crystal size, surface area, and bandgap energy of the as-synthesized photocatalysts.

As-synthesized photocatalyst	Crystal size			BET surface area (m^2g^{-1})	Bandgap energy	
	2θ (°)	β (radians)	D (nm)		Max. wavelength	Bandgap (E_g) eV
CeO_2	28.61	0.01402	10.203	68.165 ± 0.213	385	3.21
Ag_3PO_4	33.29	0.00309	44.774	1.021 ± 0.011	515	2.41
CeO_2/Ag_3PO_4	33.26	0.00361	40.107	6.107 ± 0.019	596	2.08
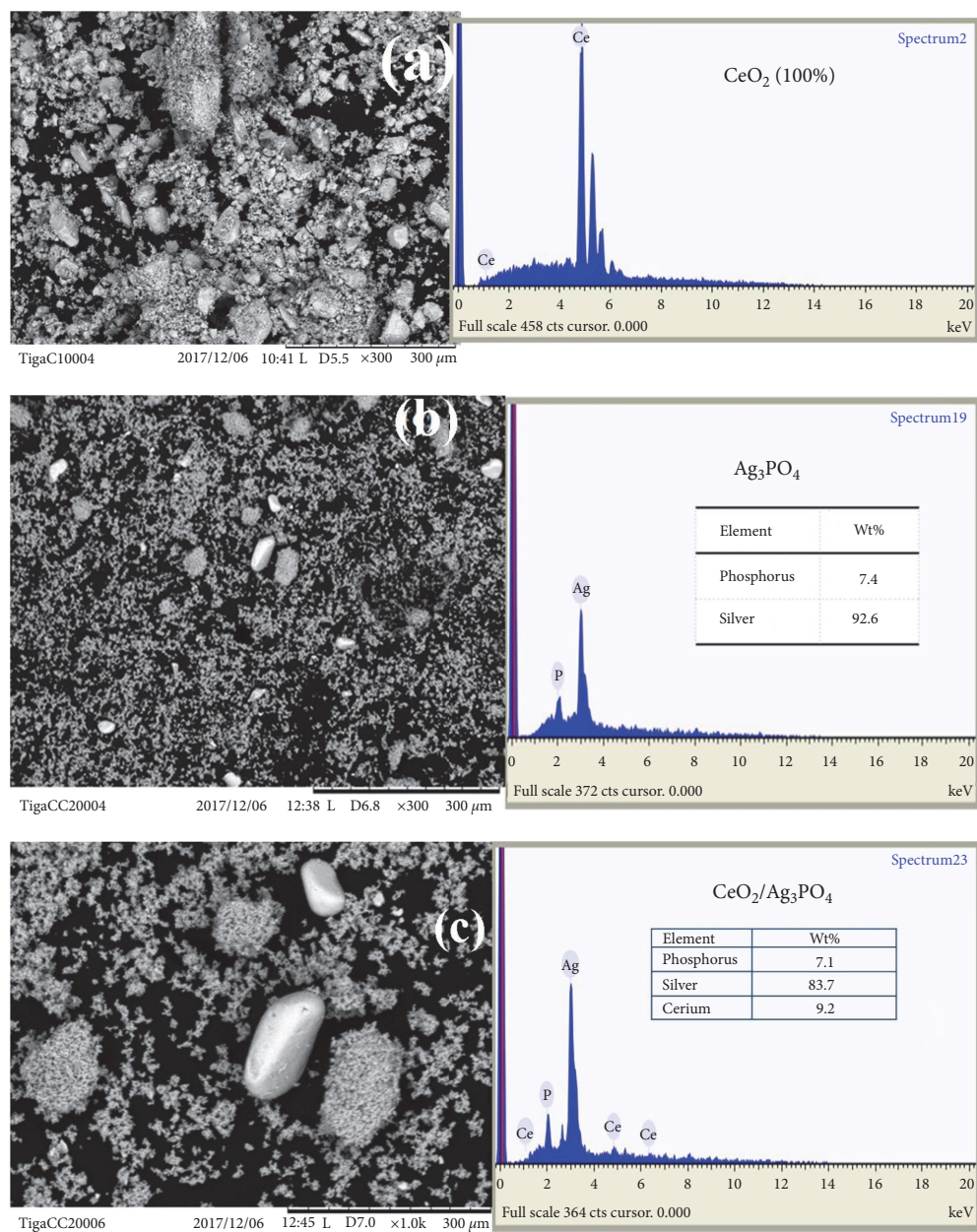
FIGURE 5: SEM-EDX images of (a) CeO_2, (b) Ag_3PO_4, and (c) CeO_2/Ag_3PO_4 photocatalyst.

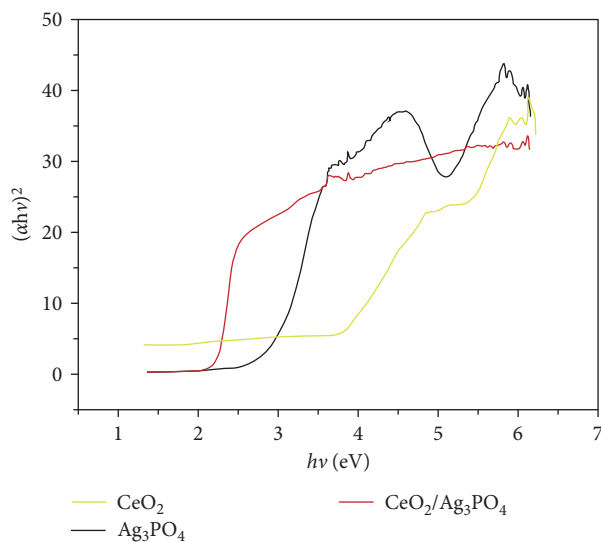FIGURE 6: Tauc plot of single (CeO$_2$, Ag$_3$PO$_4$) and binary (CeO$_2$/Ag$_3$PO$_4$) photocatalyst.

around the challenges of using a UV/vis diffuse reflectance spectrometer to obtain bandgap energy in dispersed samples. A UV–vis DRS in the 200–800 nm range was used to investigate the optical absorption characteristics of each of the photocatalysts as they were initially synthesized. By examining the optical data using Tauc's plot and the expressions for optical absorbance and photon energy hν, the bandgap values of the photocatalysts were ascertained [15, 31, 32].

$$\alpha h\nu = A\left(h\nu - E_{g}\right)^{n/2}, \tag{6}$$

where α is the absorption coefficient, which is proportional to the absorbance, h is the Planck's constant (J·s), ν is the light frequency (s^{-1}), A is the absorption constant, E_{g} the bandgap energy, and n is a constant related to the electronic interband transition.

The bandgaps of the photocatalyst was then determined by extrapolating the straight line portion of the $(\alpha h\nu)^2$ versus (hν) graphs to the (hν) axis until $(\alpha h\nu)^{1/n} = 0$ the linear section of this spectra, as shown in Figures 6 and 7. The absorption edges of the binary (CeO$_2$/Ag$_3$PO$_4$) photocatalysts are well extended to visible regions of spectrum as compared with the single nanoparticles. This may be due to the effect of modification in the electronic levels of each single nanoparticle by making them binary and ternary composite.

The bandgaps for every material as it was synthesized are shown in Table 1 based on Tauc's plot as Equation (6). It is discovered that the calculated bandgaps for CeO$_2$ and Ag$_3$PO$_4$ are 3.21 and 2.41 eV, respectively. Bandgaps of 2.08 eV exist in the binary systems CeO$_2$/Ag$_3$PO$_4$. As can be seen, the interfacial combination and matched band edges between the three semiconductors of the as-prepared nanocomposite (CeO$_2$/Ag$_3$PO$_4$) led to the formation of binary systems, which resulted in further red-shifting in the visible spectrum. The composite's ability to harvest light in the visible light region may increase as a result of the red shift's lower bandgap,

which may also contribute to electron transitions. The composite may also produce more photogenerated electron–hole pairs during the photodegradation process, which is advantageous for the photocatalytic activity.

3.1.5. FTIR Study. The functional groups of CeO$_2$ from the resulting photocatalyst were examined using FTIR in the 400–4,000 cm^{-1} range and are displayed in Figure 8 from the analysis. In the case of CeO$_2$, the band at 3,435 and 1,620 cm^{-1} corresponds to the O–H stretching vibration and the –OH scissor bending mode, respectively. These modes are caused by physically absorbed (H–bonded) water molecules or surface –OH groups [33, 34]. The C–O stretching vibration was said to be responsible for the band around 1,047 cm^{-1}, which may have been caused by extra CO$_2$ that was absorbed on the CeO$_2$ surface [35]. There are two modes of motion in the broad band at 1,315 cm^{-1}: an internal N–H bending mode and a symmetric N=O stretching mode. The N–H external bending mode is responsible for the peak at 850 cm^{-1} [36, 37]. The peaks seen at 1,387 cm^{-1} can be attributed to the N–O stretching vibration of the nitrate groups (NO$_3^-$) resulting from the precursor solution Ce(NO$_3$)$_3$·6H$_2$O used to synthesize the nanoparticle (CeO$_2$) [38]. According to Ho et al. [39], the Ce–O stretching vibration is represented by the strong band at 521 cm^{-1}.

3.1.6. Photoluminescence (PL) Study. The PL emission spectra of different photocatalysts (CeO$_2$, Ag$_3$PO$_4$, and CeO$_2$/Ag$_3$PO$_4$) were determined as indicated in Figure 9.

The PL excitation intensity decreases as a result of the photoinduced electrons and holes being effectively separated in the binary system. This is due to lower PL excitation levels, the ability of stronger bound materials to absorb photoinduced electrons, higher electron–hole separation rates, and higher photocatalytic activity [40]. Consequently, it was evident from the results of this study that the PL emission spectra of binary metal oxides were lower than those of other materials.

3.2. Photocatalytic Studies of the As-Synthesized Photocatalysts. AY is used in this study as a representative organic pollutant to test the photocatalytic activity of raw materials. Visible light is used as the radiation source. By testing the ability of each thus prepared sample to degrade AY in 160 min of visible irradiation, with an initial dye concentration of 5 mg/L and a catalyst loading of 0.15 g/L, the photocatalytic activities of each were evaluated. Using a plot of C_t/C_0 versus irradiation time, the rate of degradation was investigated. According to the results, AY decomposes and the concentration of AY decreased significantly, as evidenced by the rapid decrease of the characteristic absorption peaks corresponding to AY with increasing exposure time.

As seen in Figure 10, the degradation of the model pollutant AY under visible light irradiation was used to assess the photocatalytic performance of CeO$_2$, Ag$_3$PO$_4$, and CeO$_2$/Ag$_3$PO$_4$. A 60 min long adsorption step was allowed to take place in complete darkness before the photocatalytic reaction. In the meantime, blank tests without photocatalyst were also carried out under the same experimental conditions. Figure 11
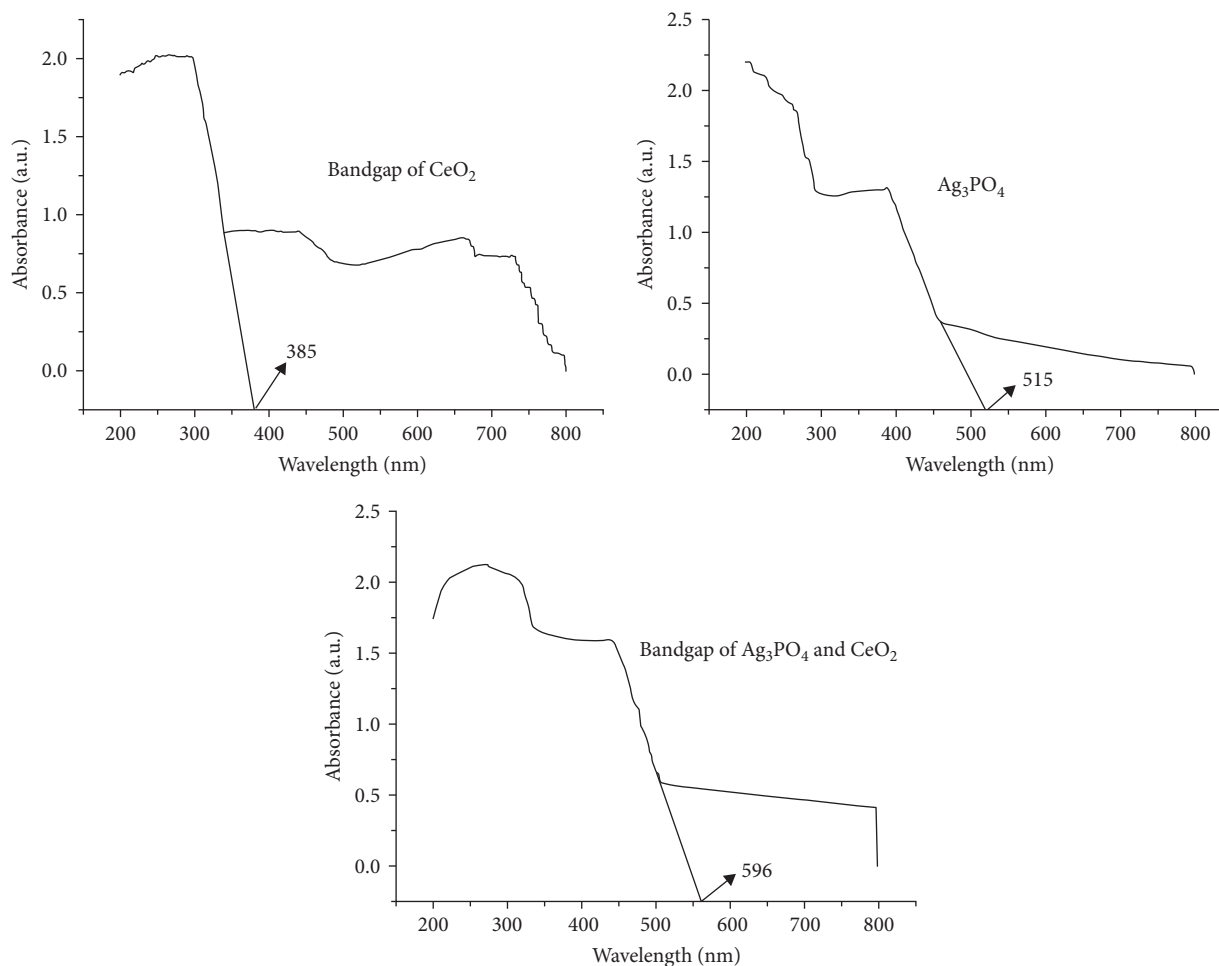
FIGURE 7: Wavelength at the maximum absorbance of each of the as-synthesized photocatalyst.
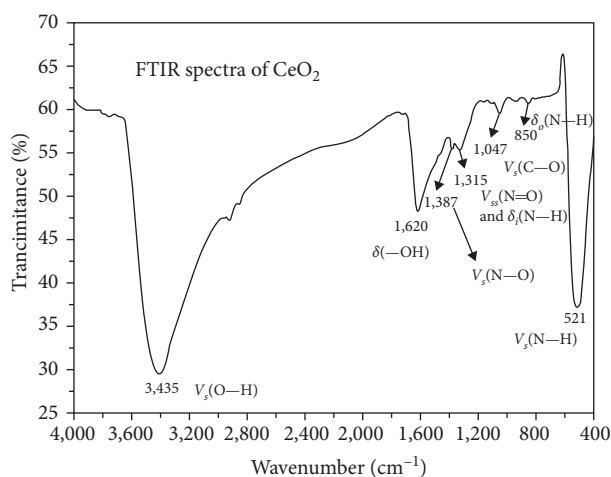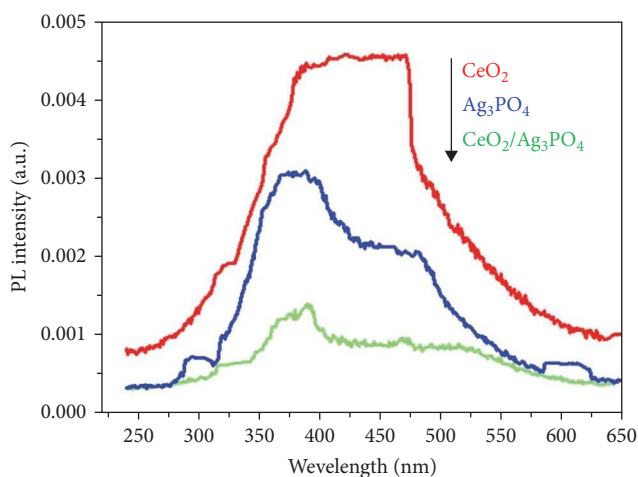

FIGURE 8: FTIR spectrum of CeO_2.

FIGURE 9: The PL emission spectra of CeO_2, Ag_3PO_4, and CeO_2/Ag_3PO_4 photocatalyst.

shows that the AY dye showed minimal degradation (<1.8%) without photocatalyst after 160 min of visible light irradiation. According to the result, CeO_2/Ag_3PO_4 > Ag_3PO_4 > CeO_2 is the order of the adsorption capacities of binary and individual

photocatalysts. The composite photocatalyst had higher photocatalytic activity than pure CeO_2 and Ag_3PO_4. In 160 min of exposure time, they decolorized 26.01% and 51.60% of AY, respectively. Pure CeO_2 have lower photocatalytic activities
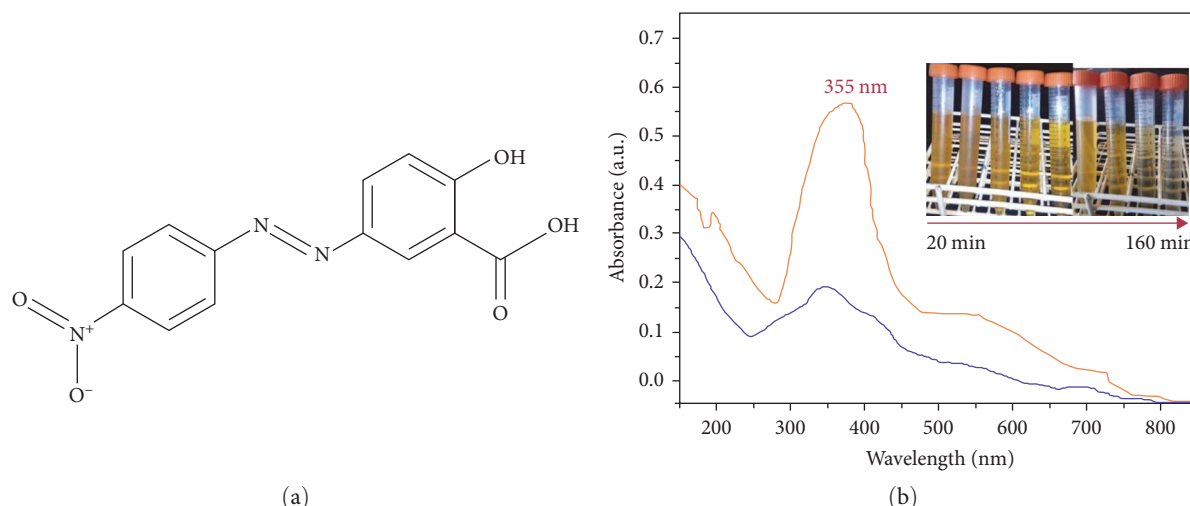
(a)

(b)

FIGURE 10: (a) Structure of alizarin yellow (b) UV/visible absorption spectra of alizarin yellow with and without the photocatalyst (after 160 min of irradiation time).
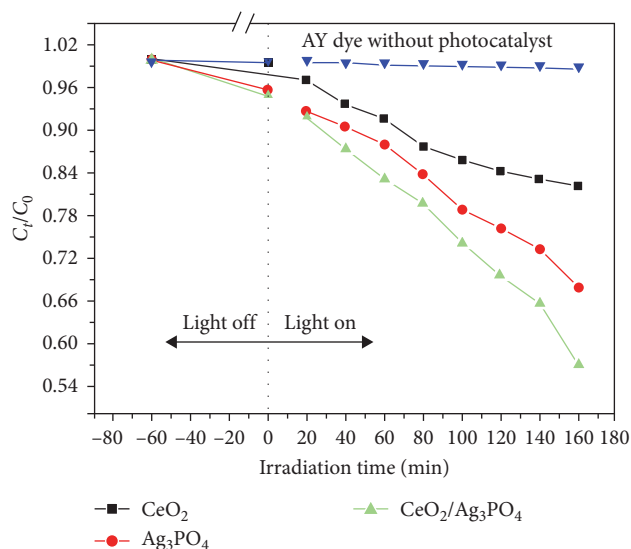

FIGURE 11: Degradation efficiency of the as-synthesized photocatalyst as function of visible irradiation time.

TABLE 2: Previous work for Ag_3PO_4/CeO_2 photocatalytic activity.

Photocatalyst	Model dye used	% of degradation	References
	Amoxicillin	65.00	[43]
	Rhodamine B	60.00	[44]
Ag_3PO_4	Methyl blue	76.00	[19]
	Rhodamine B	47.00	[25]
	Rhodamine B	59.00	[24]
	Methyl blue	98.90	[29]
	Rhodamine B	95.00	[24]
Ag_3PO_4/CeO_2	Methyl blue	76.00	[45]
	Rhodamine B	88.00	[25]
	Methyl orange	91.00	[28]
	Alizarin yellow	96.99	This work

than Ag_3PO_4 because of its higher bandgap energy, making it less sensitive to visible radiation than its single counterparts [41].

It was seen that the binary CeO_2/Ag_3PO_4 could decolorize the AY solution in 160 min of visible light irradiation, or 95.09%. Ag_3PO_4 has a higher photocatalytic degradation efficiency than CeO_2 in AY solution, which is attributed to efficient charge separation, a narrow bandgap that makes it sensitive to the visible spectrum, less electron–hole recombination, and a wide range of optical light absorption of the composite [42]. The improvement in the degradation efficiency of the binary ensemble over the single photocatalyst, as shown in Figure 11, clearly indicates that the p-n heterojunction has created a state that favors the enhancement of the degradation efficiency.

Under visible light irradiation, in the case of CeO_2/Ag_3PO_4, photogenerated electrons in CB CeO_2 can be easily transferred to the surface of Ag_3PO_4 through a heterojunction (type B), while photoinduced holes in VB Ag_3PO_4 can be migrated to the surface of CeO_2, and different electron and hole transfer pathways can effectively suppress recombination. In this way, the p-n junction formed in the p-CeO_2/Ag_3PO_4 heterostructured interface effectively separates the photogenerated electron–hole pairs, thereby increasing the photocatalytic activity of the photocatalyst [17]. Due to the reduction of Ag_3PO_4 and the resulting formation of a sandwich structure composed of Ag, Ag_3PO_4 and CeO_2, $Ag°$ metal species may be the cause [29]. As indicated in Table 2 previous work for Ag_3PO_4/CeO_2 photocatalytic activity are tasted and compared.

The kinetics of photocatalytic degradation was also demonstrated using a pseudo-first-order reaction [44]. The rate constant of the binary nanocomposite was higher than that of the individual photocatalysts, indicating the presence of a synergistic effect, as shown in Table 3. Among them, the apparent rate constants of the binary system were the highest as calculated based on the equation of $\ln(C_t/C_0)$ for the irradiation time.

TABLE 3: The apparent rate constants and % degradation of the as-synthesized photocatalysts after 160 min.

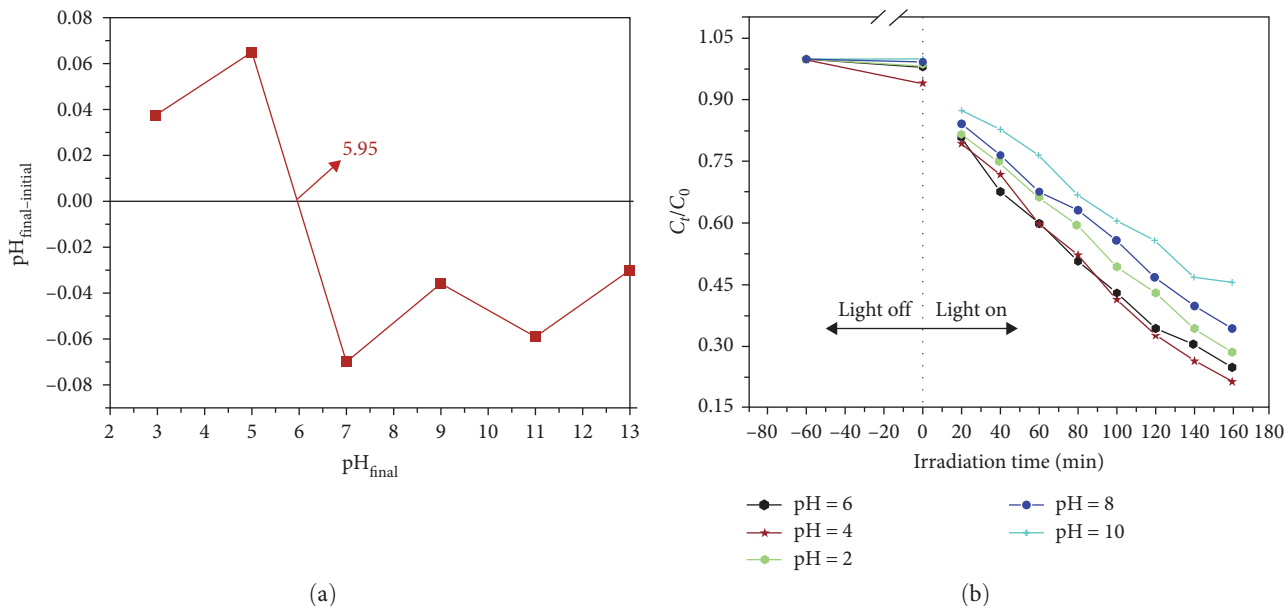| As-synthesized photocatalyst	Degradation (%)	Rate constant, k ($\times 10^{-4}$ min^{-1})
CeO_2	26.01	10
Ag_3PO_4	51.60	22
CeO_2/Ag_3PO_4	96.99	51

(a)

(b)

FIGURE 12: (a) Plot of point of zero charge of the as-synthesized binary photocatalyst; (b) effect of initial pH of the dye on the degradation of AY as a function of irradiation time (load at 0.2 g/L and initial concentration of AY at 10 mg/L).

3.3. Effect of Operational Parameters

3.3.1. Effect of pH. Figure 12(a) shows a plot of pH_{final} versus $pH_{final-initial}$. The binary photocatalyst has a pH_{pzc} value of 5.95. This shows that it has acidic nature below pH 5.95, basic nature above pH 5, and neutral pH at pH 5.95. The above photodegradation result showed that higher adsorption and higher photocatalysis were obtained at pH lower than PZC catalyst, which is pH 4.0. At this pH, there is a greater interaction between the negatively charged (anionic) AY molecules and the positively charged surface of the photocatalyst particles, which is the cause [46].

Figure 12(b) shows the degradation of an AY solution with an initial concentration of 5 mg/L and a photocatalyst loading of 0–15 g/L as a function of exposure time. At pH 4 or 95.87% and after 160 min of irradiation, binary CeO_2/Ag_3PO_4 degraded the fastest over AY solution. At solution pH 4, 6, 2, 8, and 10, the degradation rate constants (k) were 0.0163, 0.0159, 0.0098, 0.0072, and 0.0037 min^{-1}, respectively. Increased production of hydroxyl radicals due to the use of more hydroxyl anions as an alkaline medium may be to blame for the increased rate of degradation. The dye removal capacity is reduced for anionic dye adsorption when pH 4 is higher [46]. Since the surface of a dye solution tends to become negatively charged as the pH rises, the electrostatic attraction between the negatively charged dye and

the positively charged photocatalyst decreases, reducing the amount of dye that can adsorbed onto the surface.

All the obtained results confirmed that the effect of pH on AY degradation in the presence of binary photocatalyst was illustrated by degradation rate in this order:

$$pH\ 4 > pH\ 2 > pH\ 6 > pH\ 8 > pH\ 10, \tag{7}$$

at pH 4, the photocatalyst has a positive charge while AY has a negative charge. As a result, there is a strong electrostatic interaction, which causes a strong adsorption of AY molecules, bringing them close to the center of the electron–hole pair generation [47].

3.3.2. Effect of Initial Concentration of AY. By adjusting the initial concentrations of the CeO_2/Ag_3PO_4 binary solution from 5 to 25 mg/L at a fixed photocatalyst load of 0.2 g/L and pH 4, the effect of the initial concentration was investigated. The result showed that the initial dye concentration (5, 10, 15, 20, and 25 mg/L) in the binary system had an inverse relationship with the degradation rate for 160 min. When the dye concentration was 5 mg/L, it was found that after 160 min, 96.43% of the dye was removed and when the AY concentration increased to 25 mg/L, the degradation decreased to 34.98%, as shown in Figure 13. After 160 min of irradiation, the
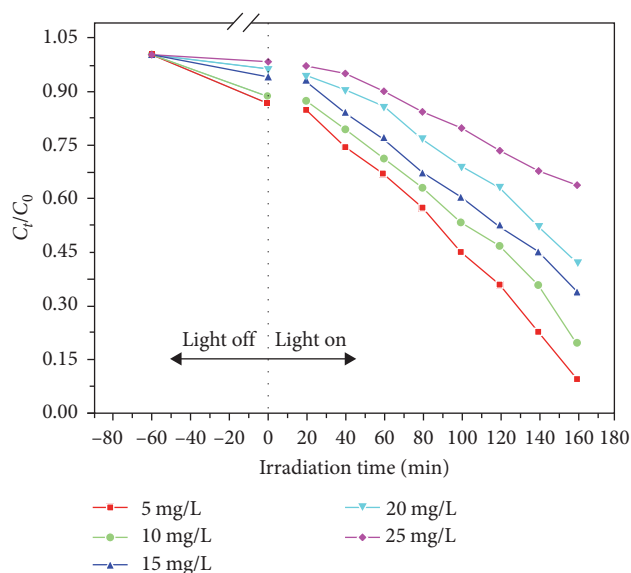
FIGURE 13: Effect of initial dye concentration on the degradation rate of AY as function of irradiation time (load at 0.2 g/L, different initial concentration and pH at 4).
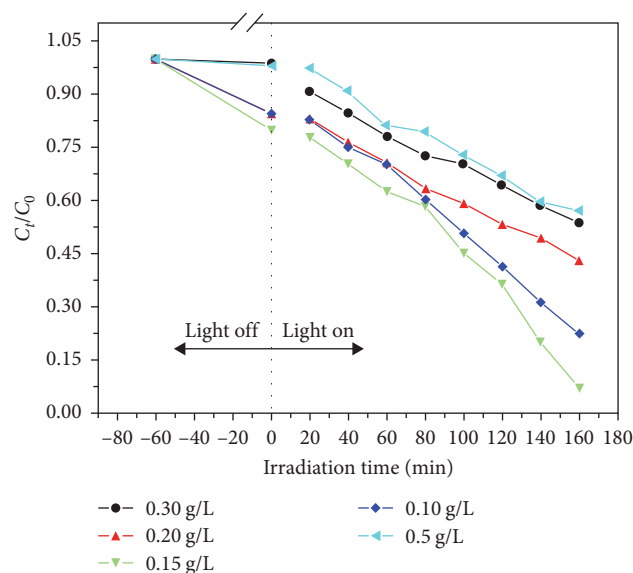

FIGURE 14: The effect of PAST photocatalyst load on AY dye degradation as a function of irradiation time (initial concentration of AY at 5 mg/L, different photocatalyst load and pH at 4).

corresponding value of the dye degradation rate constant (k) decreased as follows: 0.0163, 0.0151, 0.0101, 0.0063, and 0.0032 min^{-1}. Due to the smaller number of active sites compared with the number of AY molecules present at higher concentrations, the rate of AY degradation may have decreased with increasing concentration. The active sites may be crowded with AY molecules at higher AY concentrations, reducing the catalyst efficiency [48].

3.3.3. Effect of Photocatalyst Load. Various amounts of binary nanocomposite in the range of 0.05–0.30 g/L were used to test the impact of photocatalyst amount on the rate of AY degradation. According to Figure 14, the degradation rate increases from 0.05 to 0.15 g/L as the photocatalyst amount rises, and it further declines from 0.15 to 0.30 g/L.

With increasing photocatalyst dosage, the degradation rate of AY significantly rose from 36.09% to 96.92% and then fell to 49.88% when the dosage was excessive. At 160 min of exposure, the corresponding rate constants (k) for concentrations of 0.05, 0.10, 0.15, 0.20, and 0.30 g/L were 0.0029, 0.00136, 0.0196, 0.0106, and 0.0055 min^{-1}. The larger number of exchangeable sites available for interaction with dye molecules can be used to explain the factor that indicates increased dye adsorption with increasing adsorbent dosage [49]. Along with increasing the active functional group that is available at the adsorption site, increasing the adsorbent dose also results in an increase in surface area [50]. This lowers the total number of photons striking the catalyst particles as well as the generation of active radicals.

3.3.4. Active Species Trapping Experiments. Hydroxyl radicals ($\cdot$OH), superoxide radicals ($\cdot O_2$), and holes (h^+) were studied in order to find the active species produced in the photocatalytic reaction. The reaction mixture containing AY and photocatalyst particles was given scavengers like NaHCO$_3$, AgNO$_3$, and methanol before being exposed to visible light
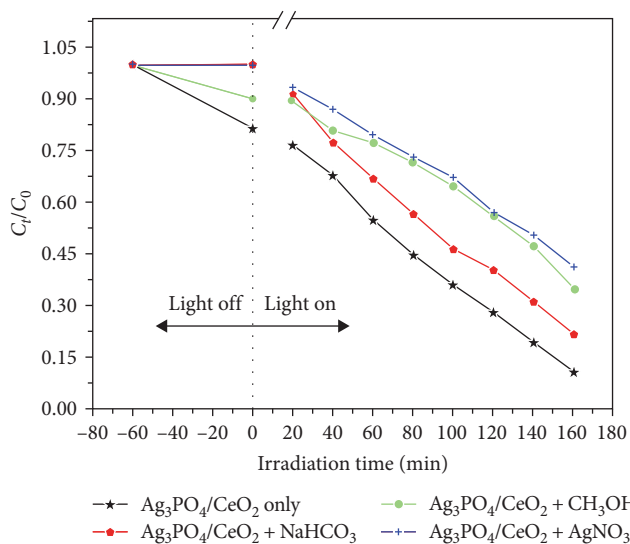

FIGURE 15: Degradation rate of AY as function of irradiation time in the absence and presence of scavengers (load at 0.15 g/L, initial concentration of AY at 5 mg/L, and pH at 4).

to undergo photocatalytic degradation. In both the presence and absence of the scavengers, Figure 15 depicts the photodegradation of AY. In the absence of scavenger, AY is degraded by photocatalysis at a rate of 96.3%. When NaHCO$_3$, CH$_3$OH, and AgNO$_3$ are added, the percentages drop to 88.72%, 68.66%, and 57.98%, respectively.

The findings showed that all of the scavengers taken into consideration reduced the efficiency of photocatalytic degradation, although AgNO$_3$ and CH$_3$OH had the strongest effects. The photocatalytic degradation of the target dye was slightly altered by the addition of NaHCO$_3$. In light of this, superoxide and hydroxyl radicals are the primary
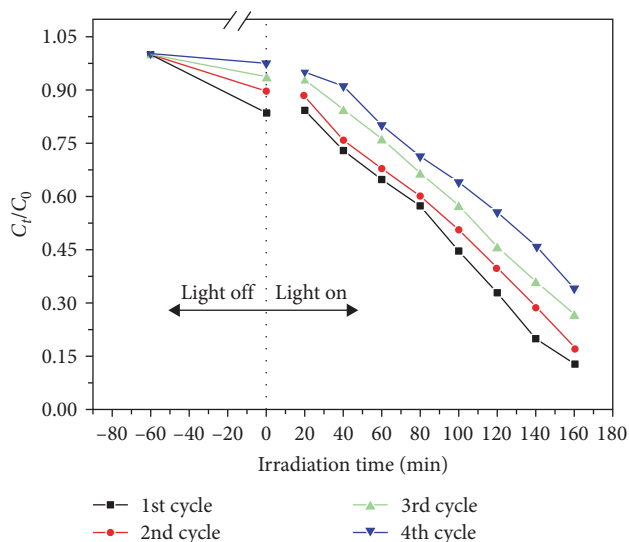
FIGURE 16: Degradation rate of AY using PAST photocatalyst as function of irradiation time in different cycles (load at 0.15 g/L, initial concentration of AY at 5 mg/L, and pH at 4).
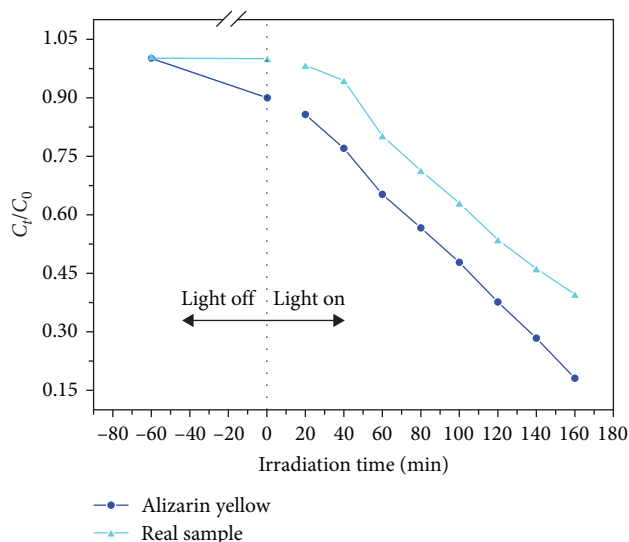

FIGURE 17: Degradation of real and model sample (AY) using PAST photocatalyst as a function of irradiation time (load at 0.15 g/L, initial concentration of AY at 5 mg/L, and pH at 4).

active species in this photodegradation reaction. $AgNO_3 >$ $CH_3OH > NaHCO_3$ is the trend for the decrease in removal rate in the presence of scavengers. It seemed that holes were only indirectly involved. Instead, the holes are involved indirectly because these species react with water molecules to produce highly reactive hydroxyl radicals [51, 52].

3.4. Photocatalytic Stability. AY was subjected to a circulation run of the photocatalytic degradation under visible light irradiation in order to assess the stability of the photocatalytic performance of binary CeO_2/Ag_3PO_4; circulation runs up to four times were possible for this process. Figure 16 illustrates how after 160 min of irradiation, the first cycle had degraded 96.01% of the dye. The rate constant (k) changed from 0.0153 to 0.0099, 0.0078, and 0.0049 min^{-1}, respectively, in the following cycles, which degraded 82.14%, 73.49%, and 54.27% of the dye, respectively. The observed decrease in degradation rate may be due to sedimentation of the dye around the catalyst after each cycle because each time the photocatalyst is reused; new regions of the photocatalyst surface become inaccessible for dye adsorption [25]. Additionally, it is probable that some photocatalyst will be lost during recycling, which will ultimately have an impact on the catalytic activity at the end of each cycle. The outcome demonstrates that after four cycles of 160 min each under ideal circumstances, the binary nanocomposite exhibits good photocatalytic performance as well as good stability.

3.5. Real Sample Analysis. The synthetic binary CeO_2/Ag_3PO_4 photocatalyst was tested for 160 min to see how well it could degrade a real sample when exposed to visible light. Figure 17 demonstrates that the percentage degradation of the aqueous solution of the model pollutant (AY) and the real sample was 96.56% and 58.87%, respectively, with a k value of 0.0170 and 0.0062 min^{-1}. According to these findings, the degradation efficiency was lower than it had been when it was optimized for the model pollutant (AY). This might be as a result of the
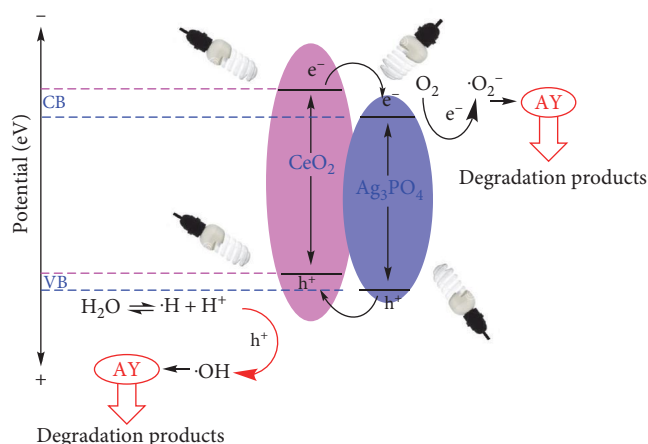
FIGURE 18: Schematic diagram of the charge-transfer mechanism of CeO_2/Ag_3PO_4 hybrids under visible light irradiation.

wastewater's different dye composition and higher concentration. It is common knowledge that cationic and anionic dyes of various types are combined in the textile industry. The degradation efficiency in a real wastewater sample was found to be lower than that of the AY model solution due to the complexity of the wastewater, which includes not only a mixture of organic dyes but also other chemicals from the bleaching steps [48, 53].

3.6. Mechanism for General Charge Transfer. A potential mechanism of charge transfer and photocatalytic degradation of the organic pollutant AY through the CeO_2/Ag_3PO_4 binary nanocomposite under visible light irradiation is presented and shown in Figure 18 in accordance with the aforementioned experimental research. The generation of electrons (e^-) in the water band (CB) and holes (h^+) in the valence band (VB) are caused by illumination of the binary nanocomposite. By calculating the flat band potentials and estimating the bandgap

energies of the relevant semiconductors, it may be possible to better understand how the photogenerated species separate. In order to achieve this, we calculated the conduction band (CB) and valence band (VB) energies of the semiconductors CeO_2, Ag_3PO_4, and CeO_2/Ag_3PO_4 using the following empirical equations:

$$E_{CB} = X - E_c - 0.5\,E_g \text{ and } E_{VB} = E_{CB} + E_g, \qquad (8)$$
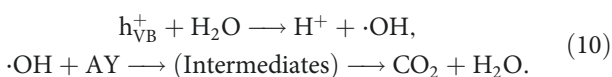
where X is the absolute electronegativity semiconductors and E_c, E_{CB}, E_{VB}, and E_g are the free electron energy on the hydrogen [29, 54].
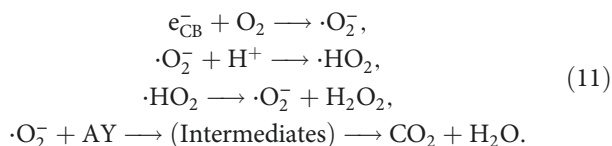
The E_{VB} and E_{CB} values of CeO_2, Ag_3PO_4, and CeO_2/Ag_3PO_4 were calculated to be 1.04, 2.66, and 2.91 eV and -1.50, -0.60, and 0.49 eV, respectively, using the equations above. In Figure 18, the energy band structure diagram of p-type Ag_3PO_4 and n-type CeO_2 is thus schematically depicted. When exposed to the photoexcited CB e^- at the CB site, molecular oxygen (O_2) creates the superoxide radical $\cdot O_2^-$, which then combines with H to create the radical species $HO_2\cdot$. Ag_3PO_4's photoinduced h^+ may react with water (H_2O) and the adsorbed AY dye molecule during its e^- transfer from CeO_2 to CB to produce the hydroxyl radical ($\cdot OH$) and the $AY\cdot^-$ anions radical, respectively. In most cases, the $AY\cdot^-$ radicals produce oxidation and reduction products. The oxidizing and reducing potential of these oxygenous radicals ($\cdot O_2^-$, $\cdot OH$, and $HO_2\cdot$) for the breakdown of organic molecules (AY) is well known [55]. The proposed photoreaction mechanism of binary nanocomposite over AY degradation under visible light is as follows:
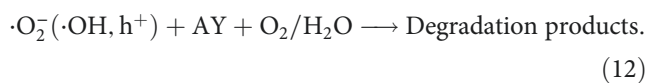
$$CeO_2/Ag_3PO_4 + h\nu \longrightarrow h_{VB}^+ + e_{CB}^-. \qquad (9)$$

Oxidative reaction:

$$\begin{aligned} h_{VB}^+ + H_2O &\longrightarrow H^+ + \cdot OH, \\ \cdot OH + AY &\longrightarrow (\text{Intermediates}) \longrightarrow CO_2 + H_2O. \end{aligned} \qquad (10)$$

Reductive reaction:

$$\begin{aligned} e_{CB}^- + O_2 &\longrightarrow \cdot O_2^-, \\ \cdot O_2^- + H^+ &\longrightarrow \cdot HO_2, \\ \cdot HO_2 &\longrightarrow \cdot O_2^- + H_2O_2, \\ \cdot O_2^- + AY &\longrightarrow (\text{Intermediates}) \longrightarrow CO_2 + H_2O. \end{aligned} \qquad (11)$$

Generally:

$$\cdot O_2^- (\cdot OH, h^+) + AY + O_2/H_2O \longrightarrow \text{Degradation products}. \qquad (12)$$
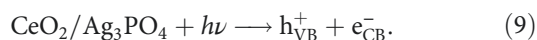
When compared with simple and binary photocatalysts, binary CeO_2/Ag_3PO_4 nanocomposite exhibits excellent photocatalytic activity in visible light. This may be due to increased charge separation and the formation of more active radicals ($\cdot O_2^-$ and $\cdot OH$). As a result, the binary nanocomposite offers high photogenerated e–h charge separation and generates a sufficient quantity of radicals for high AY dye degradation under visible light irradiation. The photocatalytic performance is influenced by (1) the photocatalysts light absorption characteristics, (2) the rates of electron and hole reduction and oxidation at the catalyst surface, and (3) the rate of electron–hole recombination [56]. Due to these elements, at the ideal pH, initial dye concentration, and photocatalyst loading under visible light irradiation, 96.99% of AY was degraded.

4. Conclusion

In this study, single (CeO_2 and Ag_3PO_4) and binary (CeO_2/Ag_3PO_4) photocatalyst were created by mixing aqueous solutions of $Ce(NO_3)_3 \cdot 6H_2O$ with NH_4OH and $AgNO_3$ with Na_2HPO_4 and the powders of single nanoparticle with Ag_3PO_4 precursors through precipitation method. Using XRD, BET, SEM-EDX, UV/vis, FTIR, and PL instruments, analyses of the photocatalysts crystal structure, surface area, morphology, bandgap energy, functional groups (bond vibration; stretching as well as bending), and optical properties were conducted, respectively.

The degradation of AY dye under visible light irradiation was investigated for the photocatalytic activities of each single and binary photocatalyst. According to the results, the binary photocatalyst exhibits the maximum adsorption capacity and degradation efficiency (96.99%) compared with each individual photocatalyst. The degradation of AY dye under the CeO_2/Ag_3PO_4 binary photocatalyst was found to be affected by solution pH, initial dye concentration, and photocatalyst loading. The results showed that 95.87%, 96.43%, and 96.92% of AY was decolorized at pH 4, initial dye concentration of 5 mg/L, and photocatalyst loading of 0.15 g/L, respectively. The scavenger effects imply that $\cdot O_2^-$ and $\cdot OH$ scavengers are key players in the degradation of AY dye. However, stability testing revealed that although the photocatalytic activity of the binary star was good, it began to decline after four reaction cycles. Both the model pollutant, AY dye solution, and the real sample collected from Kombolcha Textile Company were subjected to the photocatalytic degradation activities of binary CeO_2/Ag_3PO_4 under visible light irradiation during the study. These comparisons revealed relatively modest photocatalytic degradation efficiencies of both AY and the real sample, which were 96.56% and 57.76%, respectively.

Abbreviations

AOPs:	Advanced oxidation process
AY:	Alizarin yellow
BET:	Brunauer–Emmett–Teller
CB:	Conduction band
e_{CB}^-:	Electron in the conduction band
EDX:	Energy dispersive X-ray spectroscopy
E_g:	Bandgap energy
FTIR:	Fourier transforms infrared
h_{VB}^+:	Hole in the valance band
JCPDS:	Joint committee on powder diffraction standards
PL:	Photoluminescence

PZC: Point of zero charge
SEM: Scanning electron microscopy
UV–vis DRS: Ultraviolet–visible diffuse reflectance
                    spectroscopy
VB: Valance band
XRD: X-ray diffractometer.

Data Availability

The research-manuscript data used to support the findings of this study are included within the article.

Conflicts of Interest

The author declares that he has no conflicts of interest.

Authors' Contributions

Tigabu Bekele conceptualized and wrote the original draft, and communicated, reviewed, editid, and supervised the manuscript.

Acknowledgments

References

[1] S. Radoor, J. Karayil, A. Jayakumar, J. Parameswaranpillai, and S. Siengchin, "Efficient removal of methyl orange from aqueous solution using mesoporous ZSM-5 zeolite: synthesis, kinetics and isotherm studies," *Colloids and Surfaces A: Physicochemical and Engineering Aspects*, vol. 611, Article ID 125852, 2021.

[2] V. Selvaraj, T. Swarna Karthika, C. Mansiya, and M. Alagar, "An over review on recently developed techniques, mechanisms and intermediate involved in the advanced azo dye degradation for industrial applications," *Journal of Molecular Structure*, vol. 1224, Article ID 129195, 2021.

[3] R. Gajera, R. V. Patel, A. Yadav, and P. K. Labhasetwar, "Adsorption of cationic and anionic dyes on photocatalytic flyash/TiO_2 modified chitosan biopolymer composite," *Journal of Water Process Engineering*, vol. 49, Article ID 102993, 2022.

[4] F. E. Titchou, H. Zazou, H. Afanga et al., "Removal of organic pollutants from wastewater by advanced oxidation processes and its combination with membrane processes," *Chemical Engineering and Processing - Process Intensification*, vol. 169, Article ID 108631, 2021.

[5] T. Yildiz, H. Cengiz Yatmaz, and K. Öztürk, "Anatase TiO_2 powder immobilized on reticulated Al_2O_3 ceramics as a photocatalyst for degradation of RO16 azo dye," *Ceramics International*, vol. 46, no. 7, pp. 8651–8657, 2020.

[6] L. Liu, Z. Chen, J. Zhang et al., "Treatment of industrial dye wastewater and pharmaceutical residue wastewater by advanced oxidation processes and its combination with nanocatalysts: a review," *Journal of Water Process Engineering*, vol. 42, Article ID 102122, 2021.

[7] M. A. Al-Nuaim, A. A. Alwasiti, and Z. Y. Shnain, "The photocatalytic process in the treatment of polluted water," *Chemical Papers*, 2022.

[8] A. Naseri, G. Asghari Sarabi, M. Samadi, M. Yousefi, M. Ebrahimi, and A. Z. Moshfegh, "Recent advances on dual-functional photocatalytic systems for combined removal of hazardous water pollutants and energy generation," *Research on Chemical Intermediates*, vol. 48, pp. 911–933, 2022.

[9] Q. Gao, Y. Cui, H. Zhang, S. Wang, B. Liu, and C. Liu, "Construction of Z–scheme 1D CdS nanorods/2D ultrathin CeO_2 nanosheets toward enhanced photodegradation and hydrogen evolution," *Separation and Purification Technology*, vol. 274, Article ID 119116, 2021.

[10] A. A. Fauzi, A. A. Jalil, N. S. Hassan et al., "A critical review on relationship of CeO_2-based photocatalyst towards mechanistic degradation of organic pollutant," *Chemosphere*, vol. 286, Part 1, Article ID 131651, 2022.

[11] M. Bellardita, R. Fiorenza, L. D'Urso et al., "Exploring the photothermo-catalytic performance of brookite TiO_2–CeO_2 composites," *Catalysts*, vol. 10, no. 7, Article ID 765, 2020.

[12] A. Syed, L. S. R. Yadav, A. H. Bahkali, A. M. Elgorban, D. A. Hakeem, and N. Ganganagappa, "Effect of CeO_2–ZnO nanocomposite for photocatalytic and antibacterial activities," *Crystals*, vol. 10, no. 9, Article ID 817, 2020.

[13] A. M. A. Noman, M. A. Alghobar, and S. Suresha, "Synthesis and activity evaluation of p-n CuO/CeO_2–ZrO_2 heterojunction photocatalyst for the removal of dye from industrial wastewater under visible light irradiation," *Journal of Water and Environmental Nanotechnology*, vol. 6, no. 1, pp. 1–10, 2021.

[14] M. A. Majeed Khan, R. Siwach, S. Kumar, M. Ahamed, and J. Ahmed, "Frequency and temperature dependence of dielectric permittivity/electric modulus, and efficient photocatalytic action of Fe-doped CeO_2 NPs," *Journal of Alloys and Compounds*, vol. 856, Article ID 158127, 2021.

[15] A. M. Taddesse, T. Bekele, I. Diaz, and A. Adgo, "Polyaniline supported CdS/CeO_2/Ag_3PO_4 nanocomposite: an "A-B" type tandem n–n heterojunctions with enhanced photocatalytic activity," *Journal of Photochemistry and Photobiology A: Chemistry*, vol. 406, Article ID 113005, 2021.

[16] T. B. Mekonnen, "Synthesis and characterization of CdS/CeO_2 nanocomposite with improved visible-light photocatalytic degradation of methyl orange dye," *Journal of Plant Science and Phytopathology*, vol. 6, pp. 65–74, 2022.

[17] X. Miao, X. Yue, Z. Ji et al., "Nitrogen-doped carbon dots decorated on g-C_3N_4/Ag_3PO_4 photocatalyst with improved visible light photocatalytic activity and mechanism insight," *Applied Catalysis B: Environmental*, vol. 227, pp. 459–469, 2018.

[18] B. Borjigin, L. Ding, H. Li, and X. Wang, "A solar light-induced photo-thermal catalytic decontamination of gaseous benzene by using Ag/Ag_3PO_4/CeO_2 heterojunction," *Chemical Engineering Journal*, vol. 402, Article ID 126070, 2020.

[19] Y. Song, H. Zhao, Z. Chen et al., "The CeO_2/Ag_3PO_4 photocatalyst with stability and high photocatalytic activity under visible light irradiation," *Physical Status Solidi (A)*, vol. 213, no. 9, pp. 2356–2363, 2016.

[20] R. Y. Hong, J. H. Li, L. L. Chen et al., "Synthesis, surface modification and photocatalytic property of ZnO nanoparticles," *Powder Technology*, vol. 189, no. 3, pp. 426–432, 2009.

[21] O. Bechambi, L. Jlaiel, W. Najjar, and S. Sayadi, "Photocatalytic degradation of bisphenol A in the presence of Ce–ZnO: evolution of kinetics, toxicity and photodegradation mechanism," *Materials Chemistry and Physics*, vol. 173, pp. 95–105, 2016.

[22] B. Liu, X. Zhao, C. Terashima, A. Fujishima, and K. Nakata, "Thermodynamic and kinetic analysis of heterogeneous photocatalysis for semiconductor systems," *Physical Chemistry Chemical Physics*, vol. 16, no. 19, pp. 8751–8760, 2014.

[23] E. M. Saggioro, A. S. Oliveira, T. Pavesi, C. G. Maia, L. F. V. Ferreira, and J. C. Moreira, "Use of titanium dioxide photocatalysis on the remediation of model textile wastewaters containing Azo dyes," *Molecules*, vol. 16, no. 12, pp. 10370–10386, 2011.

[24] W. Zhou, W. Liu, and S. Hu, "A Z-scheme visible light-driven Ag_3PO_4/CeO_2 composite and its application for Rhodamine B degradation," *International Journal of Electrochemical Science*, vol. 15, pp. 4546–4555, 2020.

[25] W. Zhang, C. Hu, W. Zhai et al., "Novel Ag_3PO_4/CeO_2 p-n hierarchical heterojunction with enhanced photocatalytic performance," *Materials Research*, vol. 19, no. 3, pp. 673–679, 2016.

[26] S. Mustapha, M. M. Ndamitso, A. S. Abdulkareem et al., "Comparative study of crystallite size using Williamson-Hall and Debye-Scherrer plots for ZnO nanoparticles," *Advances in Natural Sciences: Nanoscience and Nanotechnology*, vol. 10, no. 4, Article ID 045013, 2019.

[27] Y. Liu, Q. Zhang, M. Xu et al., "Novel and efficient synthesis of Ag–ZnO nanoparticles for the sunlight-induced photocatalytic degradation," *Applied Surface Science*, vol. 476, pp. 632–640, 2019.

[28] O. N. Syazwani, Z. A. Mohd Hir, H. Mukhair, M. S. Mastuli, and A. H. Abdullah, "Designing visible-light-driven photocatalyst of Ag_3PO_4/CeO_2 for enhanced photocatalytic activity under low light irradiation," *Journal of Materials Science: Materials in Electronics*, vol. 30, pp. 415–423, 2019.

[29] Z.-M. Yang, G.-F. Huang, W.-Q. Huang et al., "Novel Ag_3PO_4/CeO_2 composite with high efficiency and stability for photocatalytic applications," *Journal of Materials Chemistry A*, vol. 2, no. 6, pp. 1750–1756, 2014.

[30] X. Li, H. Huang, H. Bin et al., "Synthesis and photovoltaic properties of a series of narrow band gap organic semiconductor acceptors with their absorption edge reaching 900 nm," *Chemistry of Materials*, vol. 29, no. 23, pp. 10130–10138, 2017.

[31] P. Kubelka and F. Munk, "Use of diffuse reflectance spectroscopy for optical characterization of un-supported nanostructures," *Journal of Applied Physics*, vol. 12, pp. 593–620, 1931.

[32] T. Tauc and F. Abeies, *Optical Properties of Solids*, IOP Publishing Ltd., North Holland, Amsterdam, 1970.

[33] M. L. Dos Santos, R. C. Lima, C. S. Riccardi et al., "Preparation and characterization of ceria nanospheres by microwave-hydrothermal method," *Materials Letters*, vol. 62, no. 30, pp. 4509–4511, 2008.

[34] M. Zawadzki, "Preparation and characterization of ceria nanoparticles by microwave-assisted solvothermal process," *Journal of Alloys Compounds*, vol. 454, no. 1-2, pp. 347–351, 2008.

[35] Y. Wang, J. Zhao, T. Wang et al., "CO_2 photoreduction with H_2O vapor on highly dispersed CeO_2/TiO_2 catalysts: surface species and their reactivity," *Journal of Catalysis*, vol. 337, pp. 293–302, 2016.

[36] X. Yu, P. Ye, L. Yang, S. Yang, P. Zhou, and W. Gao, "Preparation of hexagonal cerium oxide nanoflakes by a surfactant free route and its optical property," *Journal of Material Research*, vol. 22, pp. 3006–3013, 2007.

[37] M. Prekajski, V. Fruth, C. Andronescu et al., "Thermal stability of $Ce_{1-x}Bi_xO_{2-\delta}$ ($x = 0.1–0.5$) solid solution," *Journal of Alloys and Compounds*, vol. 578, pp. 26–31, 2013.

[38] F. Salimi, M. Abdollahifar, P. Jafari, and M. Hidaryan, "A new approach to synthesis and growth of AlOOH nanocrystalline with high pore volume," *Journal of the Serbian Chemical Society*, vol. 82, no. 2, pp. 203–213, 2017.

[39] C. Ho, J. C. Yu, T. Kwong, A. C. Mak, and S. Lai, "Morphology controllable synthesis of mesoporous CeO_2 nano- and microstructures," *Chemistry of Materials*, vol. 17, no. 17, pp. 4514–4522, 2005.

[40] N. Tian, H. Huang, Y. He, Y. Guo, T. Zhang, and Y. Zhang, "Mediator-free direct Z-scheme photocatalytic system: $BiVO_4/$ g-C_3N_4 organic–inorganic hybrid photocatalyst with highly efficient visible-light-induced photocatalytic activity," *Dalton Transactions*, vol. 44, no. 9, pp. 4297–4307, 2015.

[41] W. Xiong, W. Dai, X. Hu et al., "Enhanced photocatalytic reduction of CO_2 into alcohols on Z-scheme $Ag/Ag_3PO_4/$ CeO_2 driven by visible light," *Materials Letters*, vol. 232, pp. 36–39, 2018.

[42] G. Magesh, B. Viswanathan, R. P. Viswanath, and T. K. Varadarajan, "Photocatalytic behavior of CeO_2–TiO_2 system for the degradation of methylene blue," *Indian Journal of Chemistry*, vol. 48A, pp. 480–488, 2009.

[43] X.-Q. Liu, W.-J. Chen, and H. Jiang, "Facile synthesis of $Ag/Ag_3PO_4/AMB$ composite with improved photocatalytic performance," *Chemical Engineering Journal*, vol. 308, pp. 889–896, 2017.

[44] J. Ren, Y. Chai, Q. Liu, L. Zhang, and W.-L. Dai, "Intercorrelated Ag_3PO_4 nanoparticles decorated with graphic carbon nitride: enhanced stability and photocatalytic activities for water treatment," *Applied Surface Science*, vol. 403, pp. 177–186, 2017.

[45] W. Lin, S. Zhang, D. Wang, C. Zhang, and D. Sun, "Ultrasound-assisted synthesis of high-efficiency Ag_3PO_4/CeO_2 heterojunction photocatalyst," *Ceramics International*, vol. 41, no. 7, pp. 8956–8963, 2015.

[46] M. Akgül, "Enhancement of the anionic dye adsorption capacity of clinoptilolite by Fe^{3+}-grafting," *Journal of Hazardous Materials*, vol. 267, pp. 1–8, 2014.

[47] N. K. Temel, R. Gürkan, and F. Ayan, "Photocatalytic TiO_2-catalyzed degradation of bromophenol blue-mediated Mo (VI)-peroxo complexes in the presence of SDS," *Desalination and Water Treatment*, vol. 57, no. 44, pp. 21083–21090, 2016.

[48] H. Tedla, I. Díaz, T. Kebede, and A. M. Taddesse, "Synthesis, characterization and photocatalytic activity of zeolite supported $ZnO/Fe_2O_3/MnO_2$ nanocomposite," *Journal of Environmental Chemical Engineering*, vol. 3, no. 2, pp. 1586–1591, 2015.

[49] E. Bazrafshan, A. A. Zarei, H. Nadi, and M. A. Zazouli, "Adsorptive removal of methyl orange and reactive red 198 dyes by *Moringa peregrina* ash," *Indian Journal of Chemical Technology*, vol. 21, no. 2, pp. 105–113, 2014.

[50] Y. Hamzeh, A. Ashori, E. Azadeh, and A. Abdulkhani, "Removal of Acid Orange 7 and Remazol Black 5 reactive dyes from aqueous solutions using a novel biosorbents," *Materials Science and Engineering: C*, vol. 32, no. 6, pp. 1394–1400, 2012.

[51] M. Qamar, M. Saquib, and M. Muneer, "Titanium dioxide mediated photocatalytic degradation of two selected azo dye derivatives, chrysoidine R and acid red 29 (chromotrope 2R), in aqueous suspensions," *Desalination*, vol. 186, no. 1–3, pp. 255–271, 2005.

[52] F. Li, Y. Zhao, Q. Wang et al., "Enhanced visible-light photocatalytic activity of active $Al_2O_3/$g-C_3N_4 heterojunctions synthesized via surface hydroxyl modification," *Journal of Hazardous Materials*, vol. 283, pp. 371–381, 2015.

[53] K. Guesh, Á. Mayoral, C. Márquez-Álvarez, Y. Chebude, and I. Díaz, "Enhanced photocatalytic activity of TiO_2 supported

on zeolites tested in real waste waters from the textile industry of Ethiopia," *Microporous and Mesoporous Materials*, vol. 225, pp. 88–97, 2016.

[54] S. Kaur and V. Singh, "TiO$_2$ mediated photocatalytic degradation studies of Reactive Red 198 by UV irradiation," *Journal of Hazardous Materials*, vol. 141, no. 1, pp. 230–236, 2007.

[55] S. Ameen, M. S. Akhtar, Y. S. Kim, O.-B. Yang, and H.-S. Shin, "An effective nanocomposite of polyaniline and ZnO: preparation, characterizations, and its photocatalytic activity," *Colloid and Polymer Sciences*, vol. 289, pp. 415–421, 2011.

[56] J. Li, L. Zhu, Y. Wu, Y. Harima, A. Zhang, and H. Tang, "Green and low-cost synthesis of PANI/TiO$_2$ nanocomposite mesoporous films for photoelectrochemical water splitting," *Polymer*, vol. 47, pp. 7361–7367, 2006.